Enhancing Liver SPECT Image Quality: A Novel Approach to Mitigate Respiratory Motion Artifacts

Nathan Sinsoilliez, Ayman El Mannouy, Kao Visal, Roann Cysique, Corinne Barrau, Bérengère Prion, Stefan Janaqi, Vincent Boudousq, Baptiste Magnier

Enhancing Liver SPECT Image Quality: A Novel Approach to Mitigate Respiratory Motion Artifacts

Nathan Sinsoilliez[‡], Ayman El Mannouy[†], Kao Visal[†], Roann Cysique[†], Corinne Barrau[⋆], Bérengère Prion[⋆], Stefan Janaqi[‡], Vincent Boudousq[⋆] and Baptiste Magnier[‡,⋆]

[†] *Department of Computer Science & Artificial Intelligence, IMT Mines Ales*, Ales, France

[‡] *EuroMov Digital Health in Motion, Univ Montpellier, IMT Mines Ales,* Ales, France

[⋆] *Service de Médecine Nucléaire, Centre Hospitalier Universitaire de Nîmes, Université de Montpellier*, Nîmes, France

{nathan.sinsoilliez, janaqi, magnier}@mines-ales.fr, {corinne.barrau, berengere.piron, vincent.boudousq}@chu-nimes.fr

{ayman.el-mannouy, visal.kao, roann.cysique}@mines-ales.org,

***Abstract*—Single Photon Emission Computed Tomography (SPECT) imaging is pivotal for medical diagnosis, providing crucial insights into a patient's health. This medical imaging technique produces 3D images of a radioactive tracer's distribution in the body, detected by a gamma camera. SPECT is used to visualize physiological processes in organs, diagnosing various diseases, thus providing essential functional information. However, interpreting SPECT images just like other medical imaging results of organs near the lungs often encounters challenges due to artifacts induced by respiratory motion, leading to image noise and compromised quality.**

This study aims to enhance SPECT image clarity and fidelity for organs near the lungs using center of gravity estimation and event avoidance methods. By tracking respiratory movements with a motion camera, image clarity is refined. Additionally, methods to enhance image quality without the motion camera are explored. Calculating the barycenter allows for more accurate organ positioning within specific timeframes, while eliminating motion in others streamlines events. The amalgamation of these methods results in a notable reduction in motion artifacts and image blurring, with motion-corrected images exhibiting superior delineation of structures compared to uncorrected ones. This process is helpful for the surgeon targeting the injection.

***Index Terms*—SPECT, motion correction, desynchronization.**

I. Introduction

Single Photon Emission Computed Tomography (SPECT) imaging is crucial for detecting and treating cancer. Early detection is essential for effective treatment. The majority of cancers diagnosed were not detected until they had reached stage three or four, making treatment more challenging and, in some cases, less effective [1]. Therefore, advancing this field for greater diagnostic precision is essential to ensure early detection and intervention, ultimately improving patient outcomes and survival rates [2].

This paper explores methods aimed at improving the clarity of images generated by SPECT cameras. The integrity of SPECT scan results is often compromised by the patient's respiratory motion during the procedure. A typical SPECT scan lasts 20-30 minutes, during which the patient breathes normally. However, this respiratory movement induces thoracic motion [3], displacing the traceable radioactive substance emitting gamma photons. As a result, image blurring and reduced quality occur [4] [5], complicating the interpretation of scan results. Such issues pose significant challenges and can influence medical decisions based on ambiguous data, such as dosage adjustments. Specifically, respiratory motion, characterized by the involuntary movement of the liver during breathing cycles, presents a substantial obstacle to the accurate interpretation of SPECT images such as precise segmentation of the liver, accurate quantification of the radiopharmaceutical and estimation of the absorbed dose in the liver [6] [7] [8].

This work focuses on the desynchronization of events: on the one hand, the acquisitions from the machine (SPECT), and on the other, respiration. Synchronization, in this context, refers to the alignment and coordination of SPECT acquisitions with respiratory movements to operate in harmony, whereas desynchronization involves the disruption or loss of this coordinated timing between SPECT acquisitions and respiration. This allows for the resynchronization of events to correct motion blur in order to distinguish the structures.

The objective of this research is to investigate the efficacy of conventional techniques, specifically barycenter calculation and timestamp-based event filtering, in improving the quality of liver Single Photon Emission Computed Tomography (SPECT) images affected by respiratory motion artifacts. By addressing these artifacts, the aim is to enhance the clarity, sharpness, and diagnostic accuracy of liver SPECT scans, thereby improving patient outcomes and facilitating more precise clinical decision-making. In summary, this article contributes to the optimization of liver SPECT imaging protocols, aiming to enhance diagnostic imaging in hepatology by addressing respiratory motion artifacts. These efforts ultimately lead to improved diagnostic capabilities of liver SPECT scans, thereby enhancing patient care in liver disease management.

II. Methodology

In this section, the acquisition process, machinery used, and approaches to address this problem are detailed. It describes data collection, equipment specifications, and methodologies to mitigate respiratory motion artifacts in SPECT imaging.

A. Machine presentation: NM/CT 870 CZT

The NM/CT 870 CZT, a SPECT machine utilized in this study, was predetermined by the University Hospital of Nîmes.

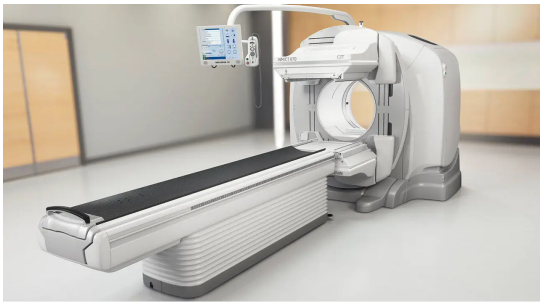

Fig. 1: Machine NM/CT 870 CZT (the GE Healthcare) [10].

The use of CZT (Cadmium Zinc Telluride) semi-conductor detectors allows for a better energy resolution and sensibility due to the direct conversion of the detected photons [9].

All data acquisition was conducted at the same place, utilizing their specified equipment. The machine operates through rotating photon cameras that encircle the patient (depicted in Fig. 1), capturing the energy and position of individual gamma photons emitted by radioactive material injected into the tumor. This process enables the imaging of the tumor's location and characteristics.

SPECT is based on the detection of gamma rays emitted by the marker as it decays. Gamma photons are detected by one or more sensors positioned around the patient. These detectors capture images, which are then utilized to reconstruct the distribution of the tracer within the body.

B. Data decryption: produced files

The NM/CT 870 CZT machine produces both List Mode and DICOM (Digital Imaging and Communications in Medicine) files. The focus here is on the List Mode files, containing the history of detected photons. Additionally, reference was made to the document "List Mode data file specification for NM GP 600 & 800 Series review 5.0" for assistance in reading and editing the files.

The List Mode file, depicted in Fig. 2, is a binary file. Its structure comprises blocks containing time, motion, and event records. Each block starts with a time record indicating photon detection time, followed by a motion record detailing photon movement, and an event record corresponding to the time record, capturing specific events. It's worth noting that some blocks may lack a motion record.

C. Events filtering: artificial stabilization

The main idea behind improving the final tumor image involves an attempt to artificially stabilize it, inspired by a well-known physics phenomenon called the "Wagon-wheel effect". When observing moving cars, either with the naked

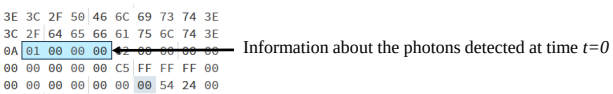

Fig. 2: List Mode file displaying example.

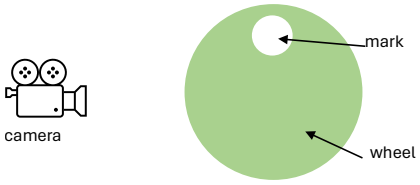

Fig. 3: A wheel with a white mark being recorded by a camera for an artificial test simulating respiration.

eye or through video, it's common to notice that at high speeds, the car wheels appear to spin backward, remain stable, or spin in the "correct" direction at lower speeds. However, observing them at their actual speed and direction is rare. This optical illusion arises from the speed at which cameras capture images or eyes process information (refresh rate). For instance, consider a basic wheel with a mark on it, as shown in Fig. 3.

Now, let's set the wheel in motion while maintaining a constant rotation speed. Let T_{wheel} represent the duration for the wheel to complete one full rotation. The camera captures images at regular intervals of time T_{camera}. In the first scenario, which is the most familiar, the wheel rotates very slowly compared to the camera, thus $T_{\text{wheel}} \gg T_{\text{camera}}$. In this instance, we can discern the positions captured by the mark in nearly every frame, as depicted in Fig. 4(a).

The situation becomes more interesting when the wheel spins rapidly, such that $T_{\text{wheel}} \leq T_{\text{camera}}$. For instance, if the wheel completes one full rotation in $T_{\text{wheel}} = 1s$ (second), while the camera captures a picture every $T_{\text{camera}} = 4.9s$, the wheel completes four full rotations, and requires an additional $0.1s$ to finish the fifth rotation between two consecutive pictures. In this scenario, the images captured by the camera will resemble those depicted in Fig. 4(b).

The phenomenon becomes particularly engrossing when the relationship between T_{wheel} and T_{camera} aligns with the principles of the Nyquist-Shannon sampling theorem, indicating a critical synchronization between the rotational speed of the wheel and the capture rate of the camera (see [11]). In this case, irrespective of the wheel's rotational speed, it will appear stationary and immobile to the camera. This synchronization between the wheel's rotational speed and the camera's capture rate is referred to as harmony.

This paper leverages this concept as a primary tool for

(a) Wheel rotating slowly compared to the camera.

(b) Wheel rotating rapidly compared to the camera.

Fig. 4: Wheel rotation and camera capture rate scenarios.

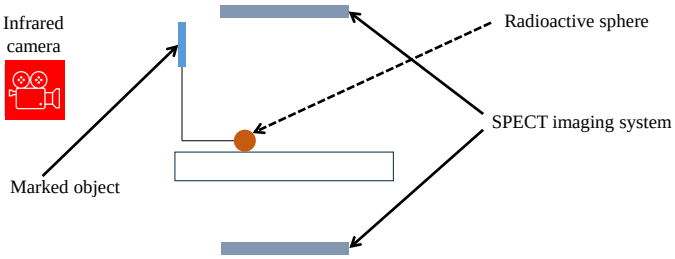

Fig. 5: The configuration of breathing simulation

tumor stabilization. The objective is to capture "snapshots" of the patient at consistent positions, achieving synchronization between the CZT camera and the patient's respiratory cycle.

D. Respiratory motion simulation setup

To facilitate the objectives, it was imperative to employ a subject with a known size and shape of the tumor. This ensured that any modifications made to enhance the image could be accurately compared to reality. Therefore, a respiration simulation was conducted using a sphere filled with radioactive material emitting gamma photons. This sphere was connected with a mechanism to a square-shaped marked object for detection by the motion camera detector, as shown in Fig. 5.

Once everything was set up, the sphere was placed in a sinusoidal motion, oscillating back and forth horizontally between the right and the left. The acquisition was then initiated with both the camera and the machine. For better precision, attempts were made to start both devices simultaneously. However, this process was manual and there was no direct connection between the camera and the machine. Consequently, the launch was not synchronized, resulting in a small delay between the two, which will be discussed further in this paper.

The image presented in Fig. 9(a) is the result of this simulation. Notice that the sphere's movement causes it to appear more like an oval than a circle, effectively demonstrating how SPECT images can be blurred due to respiratory motion.

Thanks to the graph in Fig. 6, the relative position of the marked object is observed at nearly every millisecond. The exact values of this curve are not critical; what matters is the variation. Since this object is linked to the sphere, the graph enables identification of the sphere's position. For example,

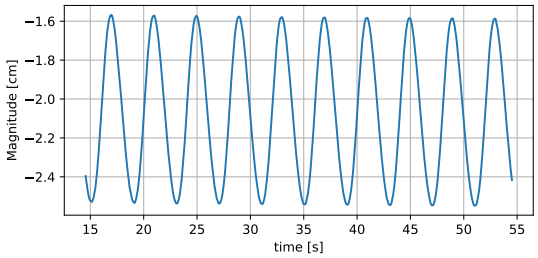

Fig. 6: The output signal captured from the camera recording the radioactive moving sphere.

Fig. 7: Sphere's position variation and speed representation.

when the curve is at its local minimum, the sphere is at the top right. When the curve reaches its maximum, the sphere is at the top left. If the curve is at its average value, the sphere is in the middle. Notice also that the curve is sinusoidal, consistent with the oscillatory movement of the sphere.

III. SPECT Image Enhancement Techniques

Here, the operations performed to enhance the quality of the image are presented along with the theory behind them.

A. Discussion about event filtering

As discussed in Sec. II-C, the main goal is to take photos of the subject when they are in the same position every time. However, the practical application is more complex as it involves a small amount of radioactive matter emitting gamma photons, fewer in number than a standard camera in daylight.

To address this issue, the acquisition time needs to be increased. The machine detects photons every 1 ms, with an estimated average of 10 photons per *ms* (millisecond), which is very insufficient. Therefore, when it is said that the acquisition time will be higher, it is also necessary to consider which moments will be the most interesting to capture.

Given a sphere with sinusoidal oscillation, the focus can be on the moments when the speed of the sphere is the slowest. The initial signal can be written as a mathematical function:

$$u(t) = \cos(\omega t), \tag{1}$$

where t represents the time in seconds (s) and ω (in units of s^{-1}) is the oscillation frequency, indicating how many times it reaches the left or right side in a second.

The speed of this signal is its derivative:

$$v(t) = \frac{du}{dt} = -\omega \sin(\omega t). \tag{2}$$

The interesting moments are when $v(t) = 0$: $\sin(\omega t) = 0$. This simplifies to:

$$t = k\frac{\pi}{\omega}, \quad \text{for integer } k. \tag{3}$$

Experimentally, when the corresponding curves are plotted, it becomes apparent that at zero velocity, the signal coincides with its maximum or minimum values. This confirms that the sphere is imaged at the critical junctures of its oscillation—precisely when it is momentarily stationary, as illustrated by the signals and dots in Fig. 7.

The same principle applies to real patients, as their organs are more stable at the end of expiration and the beginning of inhalation –this being a motivation for this work– or at the end of inhalation and the beginning of expiration. Experience with respiratory signals has shown that the expiration phase is

slower than the inhalation phase, which is why the focus is on this phase. As discussed bellow, the consistent aim is to select the signal's troughs rather than its peaks for this reason.

B. Events filtering using the breathing curve

To identify the moments in the signal troughs, the signal is plotted and an arbitrary threshold is selected. This threshold is set high enough to capture sufficient events for a clear image but low enough to "immobilize" the sphere, as recalled by the curves and dots in Fig. 7. Events occurring when the signal is above the threshold are then filtered out, as illustrated in Fig. 8. Experimentally, this is done after modifying the List mode file, then, the DICOM file is generated, allowing the visualization of the target image, as in Fig. 9(b). Notice that this image appears more circular and less wide compared to the image in Fig. 9(a). However, it still does not look perfectly circular. This outcome was expected due to the filtering process. Since the motion camera and the SPECT machine are not synchronized, there is a delay between the respiratory signal recorded by the camera and the actual respiratory motion, which follows the machine's time scale. Consequently, when attempting to select only the events occurring at the bottom of the curve, this delay causes the capture of events from a different, faster, and less stable position. This is why alternative methods for capturing respiratory motion were sought, which will be explained in the following subsection.

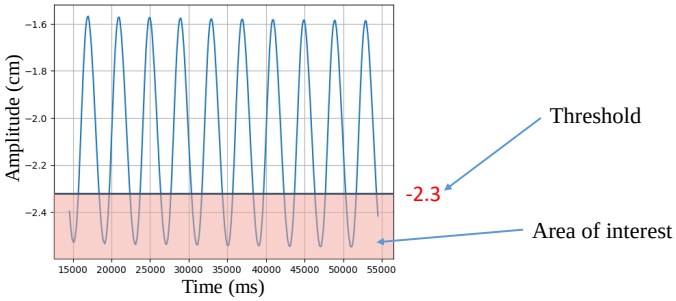

Fig. 8: Key events highlighted in the respiratory signal.

C. Extraction and event filtering using photon barycenter

In this section, the utilization of the photon barycenter for extracting and filtering respiratory signals from the list mode file is explored. The process involves calculating the center of mass of detected photons and leveraging the movement along the y-axis to derive a respiratory signal. The goal here is to apply the same event filtering method used in the previous section. This time, however, the respiratory signal is extracted solely from the list mode file.

Each frame of the SPECT machine lasts 1 *ms*, capturing the position (x, y) of the detected photon and its energy E_c (for this work, the focus is solely on the position, as the energy is not required). For each detected photon, a weight of 1 is assigned. The coordinates of the center of mass (barycenter) are calculated by:

$$(x_G, y_G) = \frac{1}{n} \sum_{i=1}^{n} x_i, \sum_{i=1}^{n} y_i, \tag{4}$$

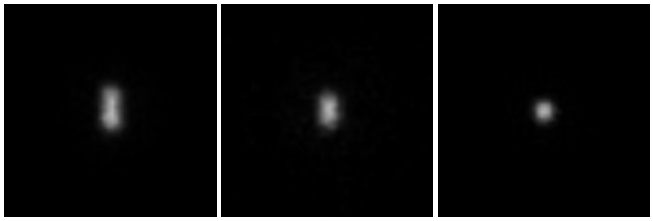

(a) SPECT image by simulating movement (b) SPECT image by filtering with a threshold (c) SPECT image by computing photon barycenter

Fig. 9: The sphere image before and after event filtering.

where n represents the total number of photons detected during the frame, and (x_i, y_i) are their coordinates. This artificial mass center should be close to the true center of mass of the nuclear matter emitting gamma photons, provided there is a sufficient number of events. An illustration of this concept can be seen in the accompanying Fig. 10.

For the sphere, only the movement of the y_G coordinate is of interest since it moves exclusively along this axis. Therefore, the signal $y_G(t)$ is expected to represent a respiratory signal, similar to what was observed with the motion camera.

It is important to note that restricting the three-dimensional movement of the mass center of human organs in a specific area to only one dimension should yield the same result. The barycenter function of the organs can be expressed as:

$$m_g(t) = (x_g(t), y_g(t), z_g(t)), \tag{5}$$

where $m_g(t)$ is the barycenter of the organs, and $x_g(t)$, $y_g(t)$, and $z_g(t)$ are its projections on each axis.

Given that organs follow a nearly identical path in each breathing cycle in an "almost periodic" manner, it can be assumed that the movement along all axes shares the same base signal. This leads to the following formula:

$$m_g(t) = u(t)(X, Y, Z), \tag{6}$$

where X, Y, and Z are the magnitudes, and $u(t)$ is the common signal (see Eq. (1)). Since the exact values of the respiratory signal are not of concern but rather its variation, the most important component extracted from this formula is $u(t)$. This is contained in the projection along any axis. For example, $y_g(t) = Yu(t)$ effectively describes the respiratory cycle, allowing determination of when the patient is inhaling

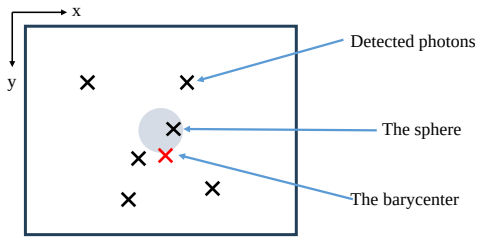

Fig. 10: Representation of detected photons and their barycenter in the SPECT machine screen.

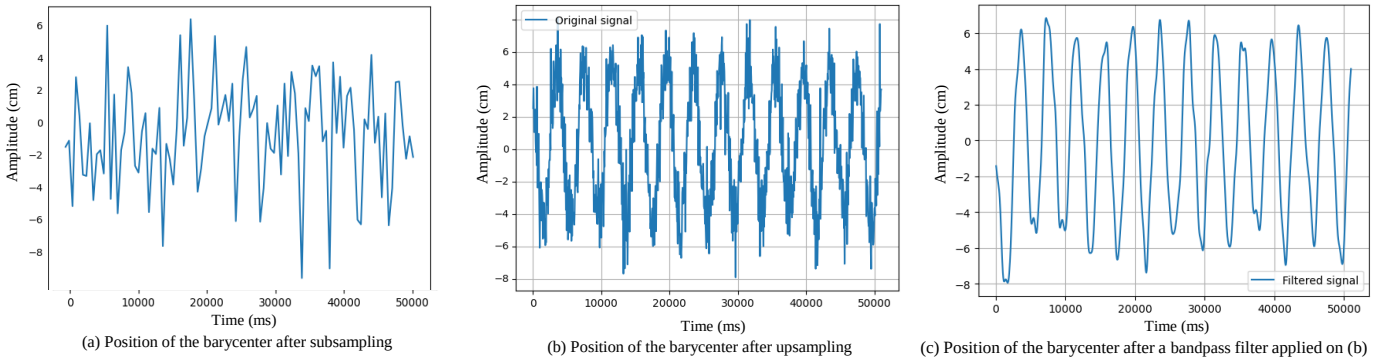

(a) Position of the barycenter after subsampling

(b) Position of the barycenter after upsampling

(c) Position of the barycenter after a bandpass filter applied on (b)

Fig. 11: Graph showing the movement of the barycenter in time at 2 different samplings, and after applying a band-pass filter.

or exhaling. The signal $y_G(t)$ obtained from the List mode file is then plotted to visualize it in Fig. 11(a).

The expected sinusoidal curve of the signal appears very noisy, attributed to two main reasons:

1) Insufficient events: Almost 10 photons per millisecond are detected, which is insufficient for clear visualization.
2) Light diffusion: This adds noise to gamma-based medical images, as photons may be redirected by nearby objects before reaching the SPECT machine detectors.

To address these issues, the acquisition time is initially extended from 1*ms* to 50*ms*. This ensures the sphere's speed is low enough for it to appear immobile during this extended period, resulting in a more periodic and readable pattern in the signal, as plotted in Fig. 11(b). Extending the acquisition time effectively mitigates the issue of event insufficiency, as evident from the graph. The new signal exhibits a more periodic and readable pattern, clearly depicting the ups and downs of the respiratory motion.

To address the noise caused by diffusion, signal filters are implemented following a Fourier transformation. Specifically, a pass-band filter with a minimum frequency of 0.2 Hz (Hertz) and a maximum frequency of 0.8 Hz is employed[12]. Those frequencies were chosen to include a whole human average respiratory cycle, between 0.2 HZ and 0.4 Hz and to take into account patient with an accelerated respiration rate due to stress or medical reasons[13]. The result is displayed in Fig. 11(c). Notice this time that the curve is much smoother and more precise. Although there are still some minor imperfections, indicating it is not an exact representation of the respiratory curve but rather an approximation. Only experimentation with this curve will demonstrate its efficiency. Utilizing this new smooth curve to substitute the respiratory signal obtained from the motion camera for filtering the desired events leads to the results shown in Fig. 9(c). The results is improved and an almost perfect circle is observed rather than a moving shape. This confirms that, even though the respiratory curve extracted from the list mode file is not perfectly accurate, it can still effectively filter the correct events at the right moments.

IV. Real Results on a Liver SPECT Image

By simulating a respiratory motion and a sphere, the application of events filtering and barycenter calculation has shown a promising result which is a significant improvement of clarity of the 3-dimension images. By removing the events –*i.e.* when the patient exhale and inhale– and calculating the barycenter of the movement of the liver, the image quality is significantly improved. In order to highlight the differences before and after desynchronization –respectively presented in Figs. 12 (a) and (b)–, the isophote lines [14] and the DoG (Difference of Gaussian) are displayed in Figs. 12 (c)-(f).

Isophotes represent curves that connect points of equal intensity in an image. They are useful for analyzing the gradient and structure of the image, as they help in understanding the intensity distribution and the shapes formed by different levels of brightness. Isophotes emphasize the areas of the image where the surface gradient is steepest, highlighting infected regions. Consequently, after desynchronization, the isophotes reveal that the target area for the surgeon is more precisely defined and more spatially concentrated. This is illustrated in Fig. 12(d), unlike in Fig. 12(c), where the slope of the image surface is more spread out and uniform.

The Difference of Gaussian (DoG) is an image processing technique that involves subtracting one Gaussian-blurred version of an image from another, less-blurred version. This method is effective for edge or blob detection and highlighting areas of rapid intensity change. It is particularly valuable for emphasizing the details and textures within an image, making it easier to identify significant features and differences between images. Like the isophotes, after desynchronization, the DoG technique allows for precise localization of the areas to be treated in the liver (see Fig. 12 (f)). In contrast, the initial image in Fig. 12 (e) shows only a single, blurry region, making it less accurate for the surgeon to identify the treatment area.

V. Conclusion

This study has demonstrated significant advancements in addressing the challenges posed by respiratory motion artifacts in SPECT imaging, particularly for organs adjacent to the lungs. Leveraging the capabilities of the NM/CT 870 CZT SPECT machine, innovative techniques such as event filtering and

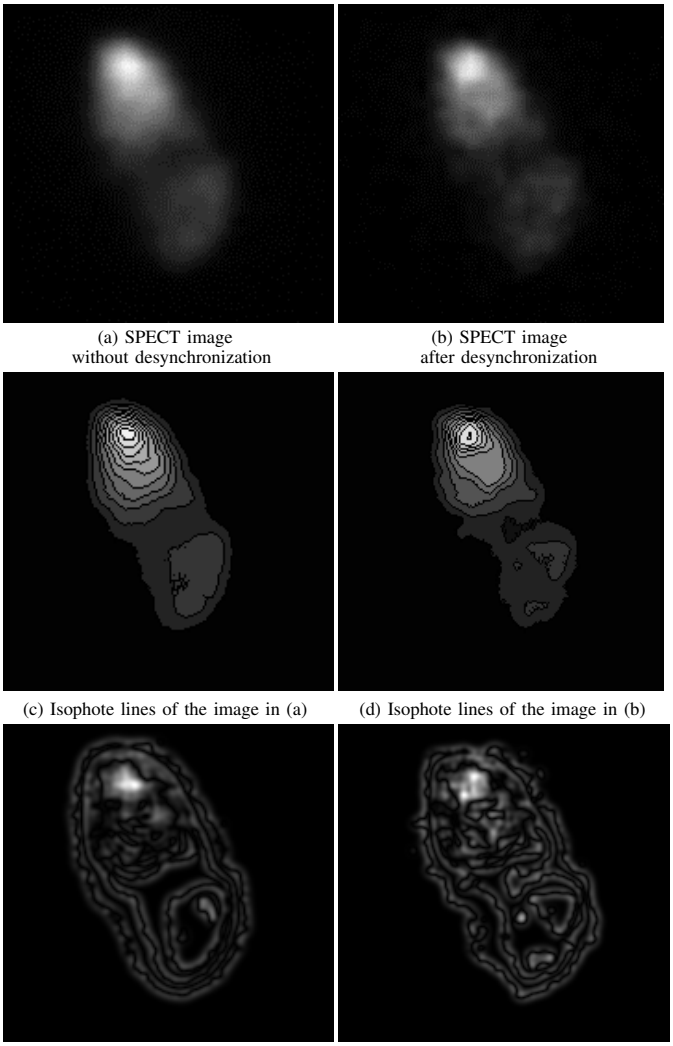

(a) SPECT image without desynchronization

(b) SPECT image after desynchronization

(c) Isophote lines of the image in (a)

(d) Isophote lines of the image in (b)

(e) DoG result of the image in (a)

(f) DoG result of the image in (b)

Fig. 12: Visual comparison of SPECT scan results of a liver.

barycenter calculations were employed to tackle the pervasive issue of image blurriness, thereby enhancing the overall clarity and diagnostic utility of SPECT scans. The corrected images exhibit notably improved structural delineation, bolstering the confidence of physicians and radiologists in interpreting SPECT images to better diagnose their patients' conditions. This research represents a pivotal step towards optimizing liver SPECT imaging, rendering it more reliable and setting a foundation for future advancements in the field. The outcomes of this investigation hold immense promise for clinical practice, empowering healthcare professionals with sharper and more detailed imaging data to guide treatment decisions effectively. The improved structural delineation observed in the corrected images underscores the tangible benefits of this approach, instilling greater confidence in medical interpretations and ultimately leading to better patient outcomes. However, an evaluation phase with practitioners or by comparing pre/post correction images and a comparison between these methods and other commercial methods will be needed to assess its usability in a clinical routine. Looking ahead, these findings serve as a catalyst for further advancements in SPECT imaging technology. Future research endeavors may explore novel methodologies for respiratory motion correction, harnessing the synergistic potential of artificial intelligence and machine learning algorithms to optimize image processing workflows and streamline clinical workflows. In essence, this study represents a significant milestone in the ongoing quest to enhance the diagnostic capabilities of SPECT imaging. By contributing to the refinement of imaging techniques and protocols, it charts a course towards a future where medical imaging plays an even more instrumental role in precision medicine and personalized healthcare delivery. This study takes pride in its role in this journey and remains committed to driving innovation and excellence in the field of nuclear medicine. Meanwhile, it is important to note that few patients have access to the List Mode file, which allows for event desynchronization, and that this capability has only recently become available with SPECT data.

REFERENCES

[1] "Cancer staging," 2022. [Online]. Available: https://www.cancer.gov/about-cancer/diagnosis-staging/staging

[2] D. Campbell, "Cancer late diagnosis: Half of patients only referred to hospital as emergency," *The Guardian*, 2014. [Online]. Available: https://www.theguardian.com/society/2014/sep/22/cancer-late-diagnosis-half-patients

[3] "Imaging artifact," *thoracic key*, 2016. [Online]. Available: https://thoracickey.com/imaging-artifacts/

[4] L. Boucher, S. Rodrigue, R. Lecomte, and F. Bénard, "Respiratory gating for 3-dimensional pet of the thorax: feasibility and initial results," *Journal of Nuclear Medicine*, vol. 45, no. 2, pp. 214–219, 2004.

[5] R. Bastiaannet, M. A. Viergever, and H. W. De Jong, "Impact of respiratory motion and acquisition settings on SPECT liver dosimetry for radioembolization," *Medical physics*, vol. 44, pp. 5270–5279, 2017.

[6] P. H. Pretorius, K. L. Johnson, S. T. Dahlberg, and M. A. King, "Investigation of the physical effects of respiratory motion compensation in a large population of patients undergoing tc-99m cardiac perfusion spect/ct stress imaging," *Journal of Nuclear Cardiology*, vol. 27, no. 1, pp. 80–95, 2020.

[7] D. Zhang, J. Sun, P. H. Pretorius, M. King, and G. S. Mok, "Clinical evaluation of three respiratory gating schemes for different respiratory patterns on cardiac spect," *Medical physics*, vol. 47, no. 9, pp. 4223–4232, 2020.

[8] A. Robert, S. Rit, T. Baudier, J. Jomier, and D. Sarrut, "Data-driven respiration-gated spect for liver radioembolization," *IEEE Trans. on Radiation and Plasma Med. Sciences*, vol. 6, no. 7, pp. 778–787, 2021.

[9] C. Desmonts, M. A. Bouthiba, B. Enilorac, C. Nganoa, D. Agostini, and N. Aide, "Evaluation of a new multipurpose whole-body CzT-based camera: comparison with a dual-head Anger camera and first clinical images," *EJNMMI Physics*, vol. 7, no. 1, p. 18, Mar. 2020. [Online]. Available: https://doi.org/10.1186/s40658-020-0284-5

[10] "Medical expo," 2024. [Online]. Available: https://www.medicalexpo.fr/prod/ge-healthcare/product-70717-1030223.html

[11] M. Unser, "Sampling-50 years after shannon," *Proceedings of the IEEE*, vol. 88, no. 4, pp. 569–587, 2000.

[12] S. Butterworth, "On the theory of filter amplifiers," *Wireless Engineer*, vol. 7, no. 6, pp. 536–541, 1930.

[13] A. Nicolò, C. Massaroni, E. Schena, and M. Sacchetti, "The importance of respiratory rate monitoring: From healthcare to sport and exercise," *Sensors*, vol. 20, no. 21, 2020. [Online]. Available: https://www.mdpi.com/1424-8220/20/21/6396

[14] D. Tschumperlé and S. Fourey, "G'MIC (GREYC's Magic for Image Computing): A full-featured open-source framework for image processing." [Online]. Available: https://gmic.eu